Laser-optimized Pt-Y alloy nanoparticles embedded in Pt-Y oxide matrix for high stability and ORR electrocatalytic activity

Riccardo Brandiele [a], Andrea Guadagnini [a], Mattia Parnigotto [a], Federico Pini [a], Vito Coviello [a], Denis Badocco [a], Paolo Pastore [a], Gian Andrea Rizzi [a], Andrea Vittadini [a,b], Daniel Forrer [a,b], Vincenzo Amendola [a,*], Christian Durante [a,*]

[a] Department of Chemical Sciences, University of Padua, Via Marzolo 1, 35131 Padova, Italy
[b] Istituto di Chimica della Materia Condensata e di Tecnologie per l'Energia ICMATE-CNR via Marzolo 1, I-35131 Padova, Italy

A B S T R A C T

The development of active yet stable catalysts for oxygen reduction reaction (ORR) is still a major issue for the extensive permeation of fuel cells into everyday technology. While nanostructured Pt catalysts are to date the best available systems in terms of activity, the same is not true for stability, particularly under operating conditions. In this work, Pt_xY alloy nanoparticles are proposed as active and durable electrocatalysts for ORR. Pt_xY nanoalloys are synthesized and further optimized by laser ablation in liquid followed by laser fragmentation in liquid. The novel integrated laser-assisted methodology succeeded in producing Pt_xY nanoparticles with the ideal size (<10 nm) of commercial Pt catalysts, yet resulting remarkably more active with $E_{1/2}$ = 0.943 V vs. RHE, specific activity = 1095 μA cm^{-2} and mass activity > 1000 A g^{-1}. At the same time, the nanoalloys are embedded in a fine Pt oxide matrix, which allows a greater stability of the catalyst than the commercial Pt reference, as directly verified on a gas diffusion electrode.
© 2024 Science Press and Dalian Institute of Chemical Physics, Chinese Academy of Sciences. Published by ELSEVIER B.V. and Science Press. This is an open access article under the CC BY license (http://creativecommons.org/licenses/by/4.0/).

1. Introduction

Polymer electrolyte membrane fuel cells (PEMFCs) have established themselves in the automotive sector, even if the widespread of PEMFC vehicles is still hindered by several issues including catalyst activity and stability [1]. Pt_xY alloys started to be investigated in the last decade as electrocatalysts for the oxygen reduction reaction, because are expected to possess the highest catalytic activity among the Pt_xM (M = rare earth) alloys according to theoretical predictions, positioning near the top of the volcano plot and close to Pt₃Ni(111) [2–4]. The activity of Pt_xM is predicted on the basis of the strain effect, which induces a downshift of the d-band center and therefore a weakening of Pt–O bond strength, with respect to pure Pt, that results in an increased oxygen reduction reaction (ORR) activity [5–7]. However, easy and scalable synthesis routes of Pt_xY are hampered by the high oxygen affinity of yttrium and

the very negative reduction potentials of −2.37 V for Y³⁺/Y as opposed to +1.2 V for Pt²⁺/Pt. Furthermore, even if the most careful conditions to avoid oxygen and water in the reaction environment are adopted, the formation of Pt/Y₂O₃ film or NPs is almost inevitable once the catalyst is exposed to air or to aqueous electrolyte [8,9]. Yttrium oxide is then easily dissolved in the harsh operating conditions, leading to Y release and progressive pauperization of the Pt-Y nanoalloys, with a concomitant decrease of the performance [5,10,11]. Notwithstanding, Pt_xY NPs, with a degree of purity and certainty in the composition, were synthetized with high energy synthetic methods or drastic reduction at high temperature under H₂ atmosphere [5,12–16]. Similarly, the superior catalytic activity was experimentally confirmed [5,12–16].

However, the current research on PEMFC development is also focusing on the enhancement of fuel cell reliability and durability, since high catalytic activity is necessary but not sufficient for the implementation in PEMFC. Several factors can reduce the lifetime of PEMFCs, including dissolution and sintering of platinum particles, corrosion of carbon support, and membrane thinning [17–22]. Carbon is largely employed as catalyst support in PEMFC

because of its large surface area, hierarchical pore structure, and high electrical conductivity. However, during fuel cell operational conditions, mainly during start-up and shutdown, the carbon support in the cathode encounters severe corrosion [19,23]. Many methods have been proposed in literature to address these problems, including using carbide, nitride, or metal oxides as catalyst supports [24–26]. Several metal oxides, exhibiting high surface area, have been investigated as catalyst supports, however, they are difficult to stabilize and tend to decrease the surface area due to coarsening in long-term operations. Even more importantly, they generally do not have sufficient electrical conductivity [27]. This issue could be overcome by combining the positive aspects of both types of electrode supports (carbons + oxides), resulting in composite materials with the ability to maintain the catalytic activity of the catalyst while safeguarding aspects of stability, processability and costs [28].

Another crucial aspect for PEMFC development is the ease of the synthesis method, the scalability, and the availability of raw materials. The exploitation of high-performance catalysts, such as tailored nanomaterials, critically depends on the feasibility of synthetic approaches for their production [29]. Here, the Pt_xY nanocatalysts were synthesized and optimised by an integrated laser-assisted method in liquid environment. The laser synthesis and processing of colloids (LSPC) enables the preparation of multi-component nanomaterials and the modification in situ of their size, composition, ripening, doping and amorphization [29–31]. Laser ablation in liquid (LAL) is the primary LSPC technique for the production of colloids of alloy NPs ready for integration in active substrates and matrixes for electrocatalysis, as recently demonstrated with Y-based [15,32] and Pt nanoalloys [33]. In LAL, the nanocatalyst is produced directly by the laser ablation of a bulk multimetallic plate in a pure liquid environment, with a self-standing process amenable to automation and remote control [34]. The LSPC techniques are cost-effective for noble metals like Au, Pd or Pt, because they do not require chemical precursors and have a quantitative yield without wasting unreacted precursors of precious elements [31,33]. LAL has been associated also to galvanic replacement reactions for the generation of Pt-Co nanoalloys [34]. Despite the unmatched versatility in the choice of the nanomaterials produced by LAL, controlling the size of the nanocrystals remains difficult with this technique [29,31,35]. Yet, size and strain are crucial factors affecting the ORR performances for nanocatalysts based on Pt [36,37]. Particle size correlates with the number of active sites per unit mass, and strain shifts the d-band center affecting the interaction with adsorbates, according to the d-band center theory. Hence, laser fragmentation in liquid (LFL) has been applied to Pt_xY NPs generated by LAL to reach the optimal size range and crystalline strain for ORR applications, while keeping the advantages of the LSPC approach in terms of scalability, low-cost and sustainability of the process, especially concerning the use of bulk materials instead of the more expensive chemical precursors and the operation at ambient conditions. Noticeably, the combined LAL-LFL synthetic method allowed the unprecedented formation of Pt_xY NPs dispersed in a nanometric thin Pt oxide matrix, which was able to avoid particles coalescence and the release of Pt_xY NPs, with a tangibly increase of the stability during the catalytic action, as confirmed in accelerated degradation tests mimicking PEMFC operational condition.

2. Experimental

2.1. Pt_xY NPs synthesis

LAL was performed with 1064 nm (6 ns, 50 Hz) laser pulses focused to 8 J cm^{-2} with an f = 10 cm lens on a bulk Pt:Y 70:30

at% plate (99.9% pure, 10 mm × 15 mm × 1 mm, Goodfellow) dipped in a cell containing pure ethanol (HPLC grade, Carlo Erba) under Ar atmosphere. The ablated target area was set to a 3 mm × 3 mm square by mounting the cell on a motorized XY scanning stage (Standa) managed with a 2-axis stepper, a DC motor controller and a custom-made LabView program.

For the LFL experiment, the NPs solution (LAL sample) was concentrated in a rotating evaporator until reaching an absorbance of 0.45 at 355 nm (in a 2 mm quartz cell). Then, LFL of the NPs solution was performed by fluxing the liquid through a glass channel (diameter of 1.5 mm) at a velocity of 0.4 mL min^{-1}. Laser pulses at 355 nm (6 ns, 10 Hz) from the triplicate of a Q-switched Nd-YAG laser were focused on the glass channel at a final fluence of 1200 mJ cm^{-2} (PtY-LFL_A sample) or 1300 mJ cm^{-2} (PtY-LFL_B sample). The PtY-LFL_Bx2 sample was fluxed and irradiated a second time at 1300 mJ cm^{-2}.

Finally, the NPs samples were washed in 1 M H_2SO_4 at room temperature. PtY NPs were then separated by vacuum filtration on a nylon nanometric filter (GVS, nylon 0.2 mm, 47 mm membrane diameter) to remove the acid solution containing the leached metals. After the separation, the NPs were washed in a Büchner with 100 mL of a 1 M H_2SO_4 solution at room temperature (25 °C). The resulting nanoparticles were thoroughly rinsed with 400 mL of ultra-pure water and 100 mL of ethanol. The resulting NPs were then dispersed in ethanol and supported on a commercial high surface area carbon black.

2.2. Physico-chemical characterization

TEM analysis was performed with an FEI Tecnai G2 12 transmission electron microscope operating at 100 kV and equipped with a TVIPS CCD camera. STEM analysis was performed with a TEM Talos F200S G2. The ImageJ software was used to measure the size distribution for each sample. The samples for TEM analysis were prepared by evaporating NP suspensions on a copper grid coated with an amorphous carbon film.

X-ray diffraction (XRD) analysis was performed with a Panalytical XPert 3 Powder diffractometer equipped with a Cu tube (40 kV, 40 mA), a BBHD mirror, a spinner and a PIXcel detector. The samples were deposed on Si zero-background substrates by drop-casting and drying at room temperature. Crystalline phase identification and Rietveld analysis were executed with the Bruker EVA and TOPAS softwares and COD databases (COD 2,310,882 for Pt2Y, COD 1538851 for Pt3Y and COD 9008480 for Pt).

X-ray photoemission spectroscopy (XPS) measurements were performed in a UHV chamber (base pressure <5 × 10^{-9} mbar), equipped with a double anode X-ray source (Omicron DAR-400), a hemispherical electron analyzer (Omicron EA-125) at r.t., using non monochromatized Mg-Kα radiation (hv = 1253.6 eV) and a pass energy of 50 and 20 eV for the survey and the high-resolution spectral windows, respectively. The calibration of the binding energy (B.E.) scale was carried out using Au 4f as reference (B.E. Au 4f = 84.0 eV). For the characterization of the catalysts the Pt amount was determined by normalizing the intensity of the Pt 4f XPS peak for the integrated area of the C 1s photoemission peak (both corrected for the differential cross section and inelastic mean free path of photoelectrons).

2.3. Electrochemical characterization

The prepared catalysts were characterized as thin films drop-casted on a glassy carbon (GC) collector electrode. The ink used for the drop-casting was formulated by mixing 2 mL of PtY NPs, 0.2 mL of milli Q-water, 5 mL of a Nafion solution (5 wt% in EtOH) and MC as carbon support, which was added so as to obtain Pt and Y concentrations close to 27% and 3%, respectively. The ink was

then sonicated for 1 h at a temperature below 20 °C. The thin film was obtained by drop-casting 12–15 μL of ink onto the clean GC electrode and dried overnight. The catalyst ink was formulated to obtain a Pt loading on the electrode of 15 μg cm^{-2}.

The catalytic activity of PtY NPs towards ORR was evaluated by linear-sweep voltammetry (LSV) at a rotating disk electrode (RDE) in O$_2$-saturated 0.1 M HClO$_4$. The electrolyte, for the ORR test, was purged with high-purity O$_2$ gas for at least 30 min to ensure O$_2$ saturation. LSVs are recorded at a scan rate of 20 mV s^{-1} at 1600 r min^{-1}, from 0.05 to 1.05 V vs. RHE. Electrochemical measurements were carried out in a typical three-electrode cell at 25 °C, using a Biologic SP200 potentiostat/galvanostat. The GC tip of the RDE ($\varnothing$ = 5 mm, A = 0.196 cm^2) used as working electrode (WE) was preliminarily polished with diamond pastes (3 mm, 1 mm, and 0.25 mm) and sonicated in Milli-Q water for 5 min. A Pt ring (Amel instruments for Electrochemistry) was used as a counter electrode (CE). The reference electrode, to which all reported potentials are referred, was a reversible hydrogen electrode (RHE) that was freshly prepared before each experiment [38]. Before the electrochemical analysis the electrocatalysts were activated cycling in the potential range 0.05–1.3 V RHE at 50 mV s^{-1} for 50 cc or until a stable cyclic voltammetry.

The electrochemical platinum surface area (EPSA) was calculated with the CO stripping method, which consists in a cyclic voltammetry carried out after the poisoning of the Pt based catalyst with carbon monoxide. The CV is carried out after the electrochemical activation: the working electrode is polarized at 0.05 V and CO is bubbled for 20 min. Hereafter, the electrolyte solution is purged with Ar for 40 min, to evacuate all the CO non adsorbed on Pt NPs. Eventually, a CV at 20 mV s^{-1} is recorded in the range 0.05–1 V vs. RHE. The EPSA is obtained by the charge determined upon integration of the CO stripping peak and considering that a full CO monolayer takes a charge density of 410 μC cm^{-2}. The electrochemical surface area (ECSA) was calculated using the following formula.

$$ECSA = \frac{EPSA}{m_{Pt}} \tag{1}$$

where m is the mass of Pt as determined by ICP-MS analysis. The ORR kinetic current (j_k) was evaluated through RDE polarisation curves at v = 20 mV s^{-1} ω = 1600 r min^{-1}, after background subtraction (CV recorded in the Ar-saturated solution obtained with the same experimental parameters i.e., scan speed, rotation rate, potential window) and the ohmic drop compensation, evaluated by impedance method at the open circuit potential. j_k is taken at 0.9 V vs. RHE and corrected by mass transfer, according to Eq. (2).

$$j_k = \frac{j_{lim} \times j_{0.9Vvs.RHE}}{j_{lim} - j_{0.9Vvs.RHE}} \tag{2}$$

The mass activity (MA) and the specific activity (SA), are determined according to the following equations.

$$MA = \frac{j_k}{m_{Pt}} \tag{3}$$

$$SA = \frac{j_k}{EPSA} \tag{4}$$

The GDE test are carried out in an electrochemical cell based on the design proposed by Arentz & Co (A-GDE cell) combined to a Parstat 3000 A-DX potentiostat [39]. The A-GDE cell is composed of a steel body that serves also as electrical contact for applying the potential to the working electrode. The WE is a GDE and consists of a catalyst-coated carbon paper. A carbon felt was inserted under the carbon paper to improve the electrical contact between the electrode and the cell body. This could become unavoidable because car-

bon paper and Nafion membrane are sold with different thicknesses and a constraining thickness is necessary to obtain good contact between the catalyst and membrane. A Nafion membrane (Nafion 117, QuinTech) was placed between the catalyst layer and the upper body (made of Teflon) of the cell. The GDE electrode was prepared dropcating a solution of the desired catalyst. 5 mg of the PtY catalyst powder and 10 μL of Nafion solution dispersion were mixed with 1.5 mL of isopropanol and 3 mL of milliQ water. The glass vial containing the mixture was placed in the ultrasonic bath and sonicated for 30 min. The circular pieces ($\varnothing$ = 20 mm) of the GDE were punched from a larger sheet and the catalyst ink was sprayed onto the GDE. The membrane is clamped on the carbon paper and the pressure is sufficient to induce a good adherence. The other side of cell, beyond the membrane, consists in a Teflon vessel containing a 4 M HClO$_4$ solution, where the CE and the RE are immersed. A graphite rod and a freshly prepared RHE were used as CE as RE, respectively. The high electrolyte concentration is necessary to reduce the solution resistance between working electrode and reference electrode, which are separated by the Nafion membrane and to ensured sufficient proton transport. The resulting effective resistance was less than 10 Ω. Before the measurements, the electrode was purged from the backside (through the gas diffusion layer) with Ar gas and the catalyst was cleaned by potential cycles between 0.05 and 1.20 V at a scan rate of 200 mV s^{-1} for 50 cycles [40,41]. To determine the ORR activity, linear sweep voltammetry in anodic direction was conducted by insufflating O$_2$ through the GDE and scanning the potential at a scan rate of 20 mV s^{-1} until a stable polarization curve was observed. The polarization curves were corrected by subtracting the background recorded under Ar flow at identical scan rate and potential window. The ohmic drop was determined by using a potenziostatic electrochemical impedance spectroscopy scanning from 10 kHz to 1 Hz at the open circuit potential with a superimposed sinusoidal potential with amplitudine of 5 mV [42].

The EPSA of GDE was determined by conducting CO stripping voltammetry before and after the ADT. Before CO stripping measurements, the electrode was purged with Ar and the catalyst was cleaned through potential cycles ranging from 0.06 to 1.10 V vs RHE at a scan rate of 500 mV s^{-1} until a consistent CV was observed (approximately 100 cycles). Further specification for the GDE CO stripping procedure and accelerated stress tests are reported in SI. Unless otherwise specified, all evaluations were performed at room temperature.

2.4. Computational details

Spin-polarized density functional calculations were performed within the plane-wave pseudopotential framework, using the PWSCF code of the QUANTUM ESPRESSO suite (QE) [43]. The interaction between ion cores and valence electrons was modeled by GBRV ultrasoft pseudopotentials [44]. Valence orbitals were expanded on a plane-wave basis set with a kinetic energy cutoff of 40 and 30 Ry for variable- and fixed-cell calculations, respectively, while the cutoff on the augmentation density was 250 Ry. The PBE exchange–correlation functional was adopted [45]. For Pt and Pt$_3$Y bulks we sampled the Brillouin zone with a 10 × 10 × 10 Monkhorst-Pack grid, whereas a 6 × 6 × 6 grid was adopted for Pt$_2$Y.

Surfaces were modelled by means of a repeated slab approach, adding 16 Å of vacuum to separate the periodic images along the vertical direction. The coordinates of the atoms belonging to the two bottom layers were kept frozen. For these calculations, a $2\sqrt{3} \times 2\sqrt{3}\,R30°$ supercell was used for Pt, whereas $\sqrt{3} \times \sqrt{3}\,R30°$ supercells of similar size were used for both Pt$_2$Y and Pt$_3$Y. The surface Brillouin zone was sampled by a 2 × 2 grid

in all the cases. For all the investigated substances, the interaction with the NPs was studied by considering (111) surfaces.

3. Results

The LFL conditions were adjusted to improve particle fragmentation and reduce amorphization and dealloying, by acting on laser fluence and number of irradiation cycles. Compared to the pristine PtY-LAL sample, the LFL succeeded in shifting the size of the Pt_xY NPs below 10 nm in samples PtY-LFL_A and PtY-LFL_B, (Fig. 1a) which are obtained by laser irradiation at, respectively, 1.2 and 1.3 J cm^{-2}. The 10 nm size threshold is indicated as the best performing range for ORR with PtY based nanocatalysts [5]. Conversely, the average size of the Pt_xY NPs increases above 10 nm in the PtY-FL_Bx2 sample, which is obtained by a second irradiation cycle of the PtY-LFL_B one, due to a laser-induced ripening process [31,35]. This is well evident by the fraction of Pt_xY NPs larger than 10 nm in the size histogram of the PtY-LFL_Bx2 sample (Fig. 1a), which is the largest of all the samples after LFL or LAL.

Apart from the size evolution, all the samples show similar morphology consisting in spherical NPs embedded in a hypodense matrix of ultrafine particles in the transmission electron microscopy (TEM) images (Fig. 1a). The composition of the samples, quantified by inductively coupled plasma assisted mass spectroscopy (ICP-MS, Fig. 1c), also is comparable among samples and close to the Pt/Y 3/1 ratio of the bulk target, with a slight decrease to 2.9 in the LFL samples (see also Table S1). Noteworthy, the Pt/Y ratio is highly reproducible, as attested in three different synthesis of PtY-LFL_B (Table S1). The chemical composition at the level of

the single Pt_xY NPs and of their surrounding matrix was assessed also with energy dispersion spectroscopy (EDS) bidimensional mapping for the PtY-LAL, PtY-LFL_A and PtY-LFL_B samples (Fig. 1d), i.e., those with the smallest average size. The maps of the Pt L-line (9.4 keV, green map) and Y K-line (14.9 keV, red map) confirm the presence of the two elements in the spherical NPs, but a background of the Pt and Y signals is also found in the surrounding matrix of ultrafine particles. Noteworthy, the O K-line (0.52 keV) is present in the surrounding matrix, with a homogeneous distribution indicating that metallic Pt_xY NPs are embedded in a Pt-Y oxide network. These features are common to all the PtY-LAL, PtY-LFL_A and PtY-LFL_B samples, suggesting that their difference mainly consist in the size distribution of the Pt_xY NPs and, possibly, in their composition.

Although TEM and STEM-EDX analysis provide information on the elemental composition of the samples with nanometric resolution, these techniques can only analyse a nanoscale portion of the samples. Therefore, the accurate identification of Pt-Y nanoalloys and of the pure Pt component in the whole samples were performed with X-ray diffraction (XRD) analysis and the Rietveld refinement of the XRD patterns (Fig. 2a). All the reflections of the bulk Pt-Y target are present in the laser-generated NPs, although superimposed to the contribution of components with low crystallinity. Indeed, the crystallinity degrees estimated from the XRD patterns are of 40 wt% for the PtY-LAL sample, 37 wt% and 40 wt% for the PtY-LFL_A and PtY-LFL_B samples and only 32 wt% for the PtY-LFL_Bx2 sample (Fig. 2b). The crystalline phases are all due to the cubic Pt_3Y, Pt_2Y and Pt phases (see Table S2). Because of the shift in the diffraction peaks due to lattice expansion when Pt atoms are replaced by Y, the Pt_xY alloys can be clearly
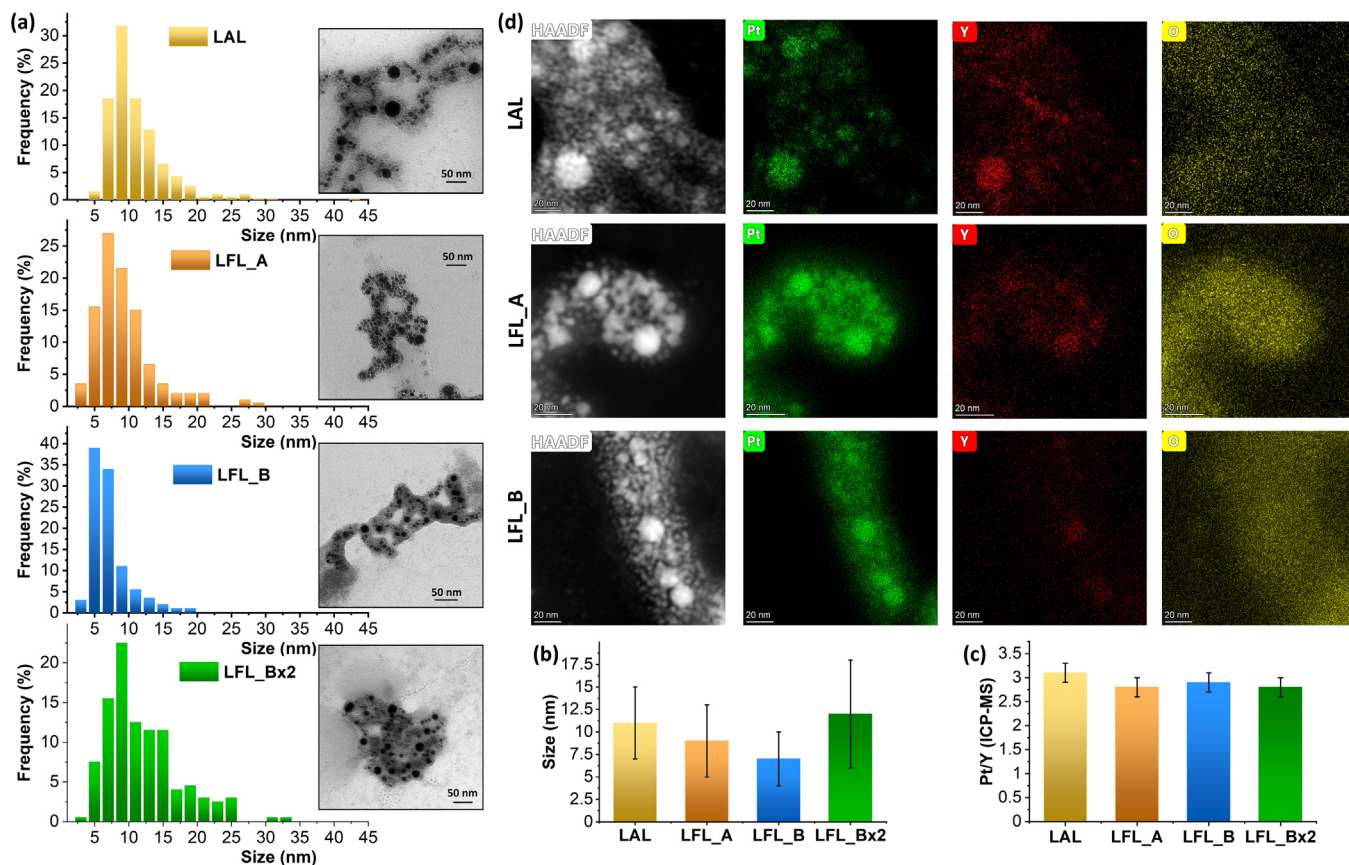

Fig. 1. Morphological and elemental characterization of PtY catalysts. (a) Representative TEM images and size distribution of the Pt-Y NPs samples; (b) Average size of Pt-Y NPs (error bars indicate the standard deviation); (c) Pt/Y ratio estimated by ICP-MS; (d) STEM-dark field and STEM-EDX maps of the Pt L-line, Y K-line and O K-line for NPs of the LAL, LFL_A and LFL_B samples.
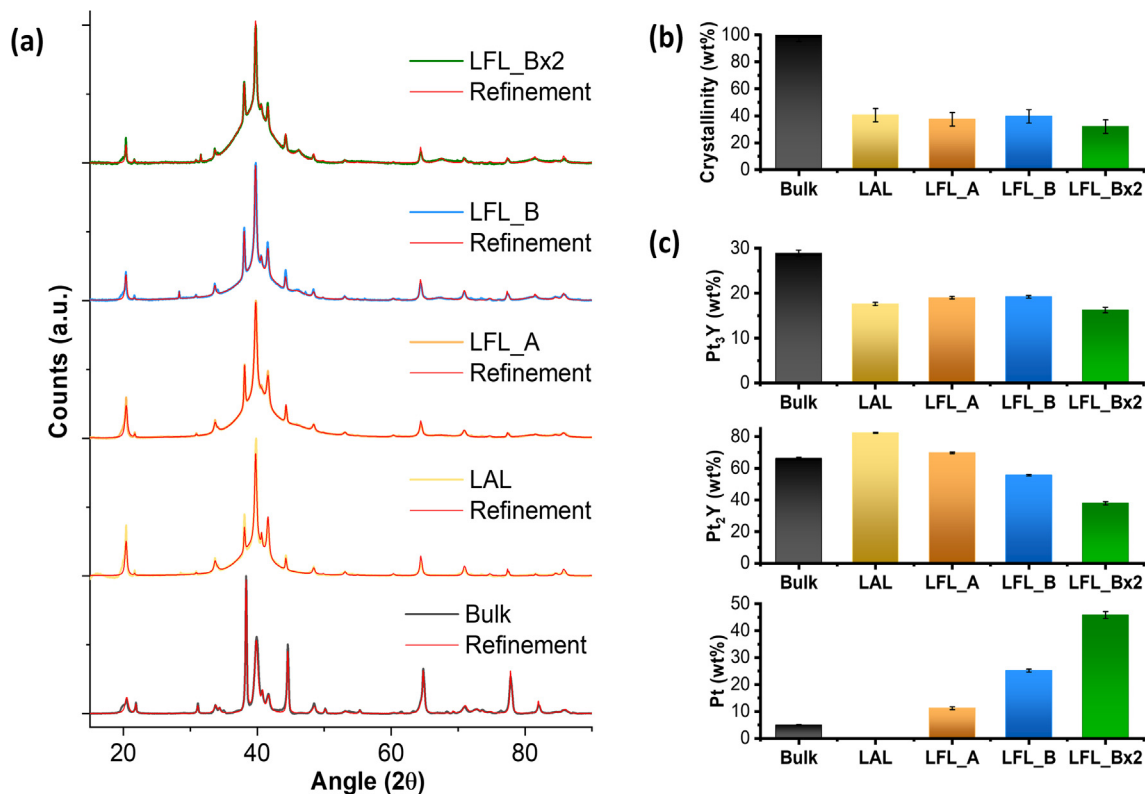
Fig. 2. Structural characterization of PtY catalysts: (a) XRD patterns and Rietveld refinement of the Pt-Y samples and the bulk target. crystallinity degree (b), and mass fraction (c), obtained from the Rietveld refinement of the XRD patterns.

discriminated from pure Pt in the diffraction patterns. In fact, the Rietveld analysis indicates that Pt_3Y is 18–19 wt% for PtY-LAL, PtY-LFL_A and PtY-LFL_B, 16 wt% for PtY-LFL_Bx2 versus the initial 29 wt% in the bulk target (Fig. 2c). The Pt_2Y fraction exhibits a more pronounced difference among the samples, with 82 wt% for PtY-LAL, 70 wt% for PtY-LFL_A, 56 wt% for PtY-LFL_B and 38 wt% for PtY-LFL_Bx2, versus the 66 wt% in the bulk target.

The pure Pt component is below 5 wt% in the PtY-LAL and bulk target samples, but increases to 11, 25 and 45 wt% for the PtY-LFL_A, PtY-LFL_B and PtY-LFL_Bx2 samples, respectively. It should be noted, however, that the volume-weighted size of Pt crystalline grains is below 5 nm for the PtY-LFL samples. Hence, the Pt phase should be mostly associated to the ultrafine NPs dispersed in the Pt-Y oxide matrix observed in TEM images. These particles are likely formed during the laser synthesis due to the oxidation of Y. In fact, in the PtY-LFL_Bx2 sample, the conversion of Pt_2Y into ultrafine Pt is the highest of all samples and the ripening of the NPs size compared to the original PtY-LFL_B sample was also observed in the TEM analysis.

The surface composition and chemical state of the Pt-Y NPs, after the chemical activation by acid wash, which is representative of the operating electrocatalysis condition, was identified with high resolution X-ray photoelectron spectroscopy (XPS, Fig. 3). For completeness, the XPS analysis was also applied to the pristine non washed sample (Fig. S1). In all the samples, after checking the adventitious carbon was at 284.8 eV, the Pt 4f spectra were deconvoluted in 3 components, the most intense peaks at 71.1 and 72.3 eV are assigned to the metallic Pt and to PtO, respectively. The doublets at approximately 74.4 eV to PtO_2 (see Table S3 for precise binding energy values and percentage of components). These values are in agreement with partially oxidized Pt nanoparticles already found in similar systems [46]. The decrease of the Pt (0) signal when going from PtY-LFL_A to LFL_B and LFL_Bx2 samples is in agreement with the TEM and XRD analysis, all indicating

the increase of the thickness of the Pt oxide matrix along the series of samples. This indicates that the thickness of the Pt oxide shell embedding the metallic Pt-Y NPs can be controlled by acting on the fluence of the laser beam and the number of LFL treatments.

The overall photoemission Y 3d peak has been rationally fitted with only one component centered at a B.E. of 158.46 assigned to Y_2O_3. The Y 3d signal obtained from the target, after sputtering, is also shown in Fig. 3(g) as a comparison. In that case, the Pt_xY alloy signal is clearly visible at about 156.2 eV, while the Y_2O_3 component is found at 158.2 eV [13]. Considering the Y(0) as belonging to the Pt-Y alloys, only the PtY-LFL_A barely shows its presence (3%) at particles surface (Fig. 3b), whereas no such evidences were detected in the LFL_B samples. Here, the Y 3d peaks show again the prevalence of a single component centered at a B.E. of 157.4 eV due to Y_2O_3.

Therefore, XPS confirms the presence of Pt-Y oxides surrounding metallic Pt_xY NPs, according to TEM, EDX mapping and XRD. Fig. S1 also reports the high-resolution Pt 4f XPS spectra of pristine samples before acid treatment. The Pt 4f XPS spectra show a similar Pt(0) concentration (65%–67%) in PtY-LAL, PtY-LFL_A and PtY-LFL_Bx2. This attests a 5% increase of the superficial metallic Pt upon removal of the oxides with a lower chemical resistance, as Y oxides, in the PtY-LFL_A sample. Instead, the PtY-LFL_Bx2 has a similar content of surface Pt(0) and Pt(II), 46% vs. 41%, since the oxidation of Y was already promoted by the double LFL treatment, leaving a thicker Pt oxide matrix embedding the nanoalloys.

4. Electrochemical kinetic analysis

The catalytic activity towards the ORR was evaluated by cyclic voltammetry and linear sweep voltammetry at rotating disk electrode in both Ar-purged and O_2-saturated 0.1 M $HClO_4$ electrolytes. Before the electrochemical characterization, the NPs were washed
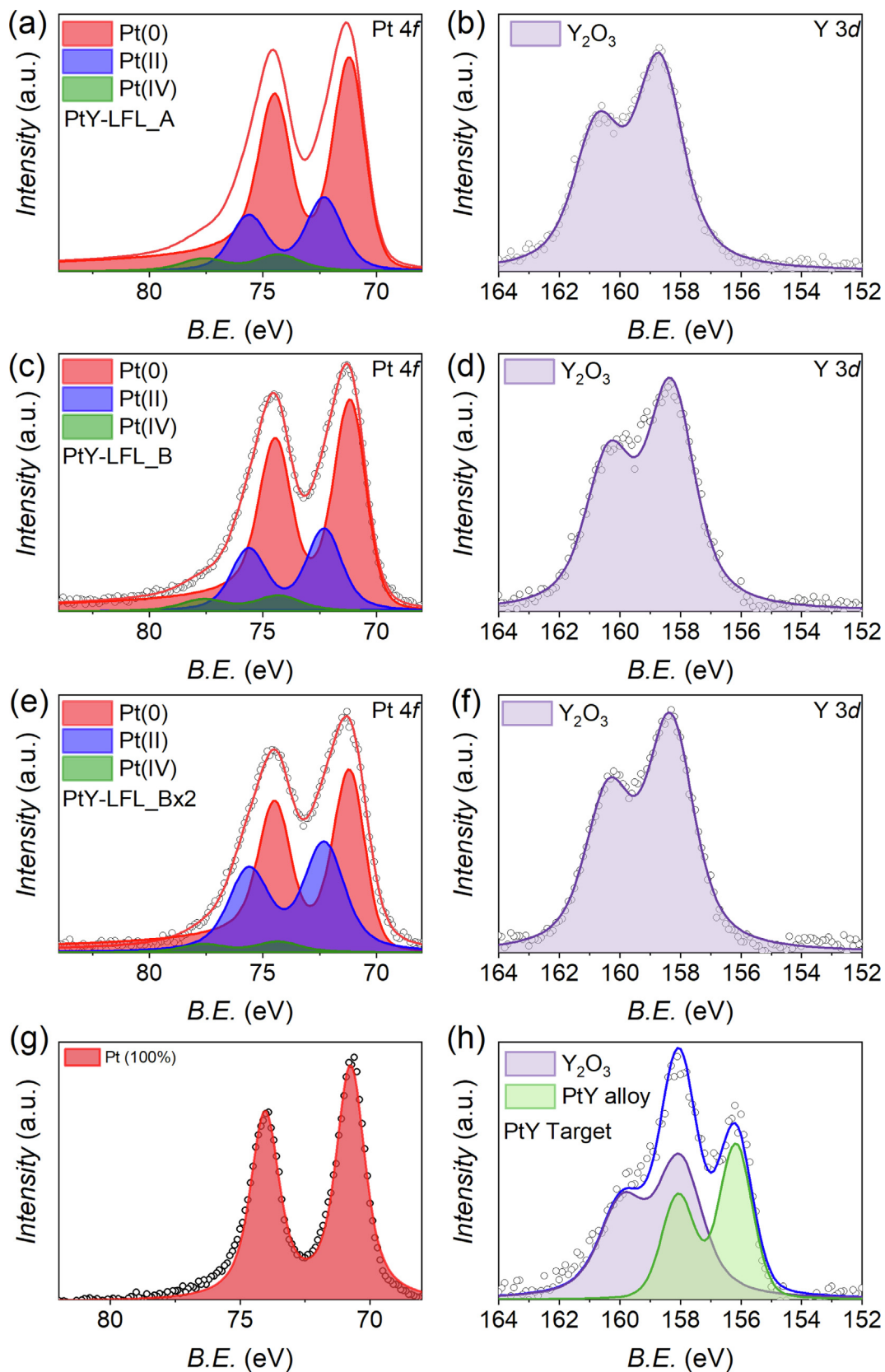
Fig. 3. High resolution Pt 4*f* and Y 3*d* XPS spectra and deconvolution of PtY catalysts after acid washing in sulfuric acid (a and b) PtY-LAL_A, (c and d) PtY-LAL_B, (e and f) PtY-LAL_Bx2, (g and h) PtY target after sputtering.

in 1 M H_2SO_4 and were supported on commercial high surface carbon black. The catalysts were also activated by consecutive voltammetric cycles at a scan rate of 50 mV s^{-1} in the potential range 0.05–1.3 V. Fig. 4 reports the effect of the chemical and electrochemical activation of the PtY-LAL catalysts. Fig. 4(a) (blue line) shows the LSV at RDE of the as prepared PtY_LAL in O_2 saturated 0.1 M $HClO_4$. If the half wave potential ($E_{1/2}$), namely the potential at the half value of the limiting current (j_{lim}), is taken as descriptor for the catalytic activity it is plane that $E_{1/2}$ is much less positive than the Pt/C TKK reference, meaning that it is required a higher overpotential at PtY_LAL than at Pt/C for triggering the reduction of oxygen. However, if the green LSV is considered, which represents the electrochemical behavior of PtY_LAL after a 10 min washing in 1 M H_2SO_4, it is obvious that the catalytic activity increases, since there is a huge increase of j_{lim} and the positive shift of $E_{1/2}$ passing from the as-prepared (blue) to the acid washed catalyst (green). Such increase of catalytic activity is because the chemical

activation in acid allows the partial removal of the exposed yttria, which dissolves at acid pH, enriching the particle surface of Pt active sites [5,10,11]. The increased activity is even more pronounced after the electrochemical activation where, the LSV for the activated catalyst (Fig. 4a, red), easily surpass the one at Pt/C. The electrochemical activation was thoroughly investigated by performing a set of CV at different inversion potential (Fig. 4c). Fig. 4(e) compares the LSV for the catalyst previously washed in acid (PtY_LAL_W) after electrochemical activation at inversion potential of 1, 1.3 and 1.4 V. It is obvious that the best activated catalyst is obtained when the inversion potential is limited to 1.3 V vs. RHE. This is further verified if we look at how the values of mass activity and specific activity vary (Fig. 4b) as well as the values of $E_{1/2}$ and kinetic current at 0.9 V (Fig. 4d). All these parameters indicate that electrochemical activation leads to the best performance by limiting the scan to 1.3 V, to the point that the catalytic activity far exceeds both that of the non-activated catalyst
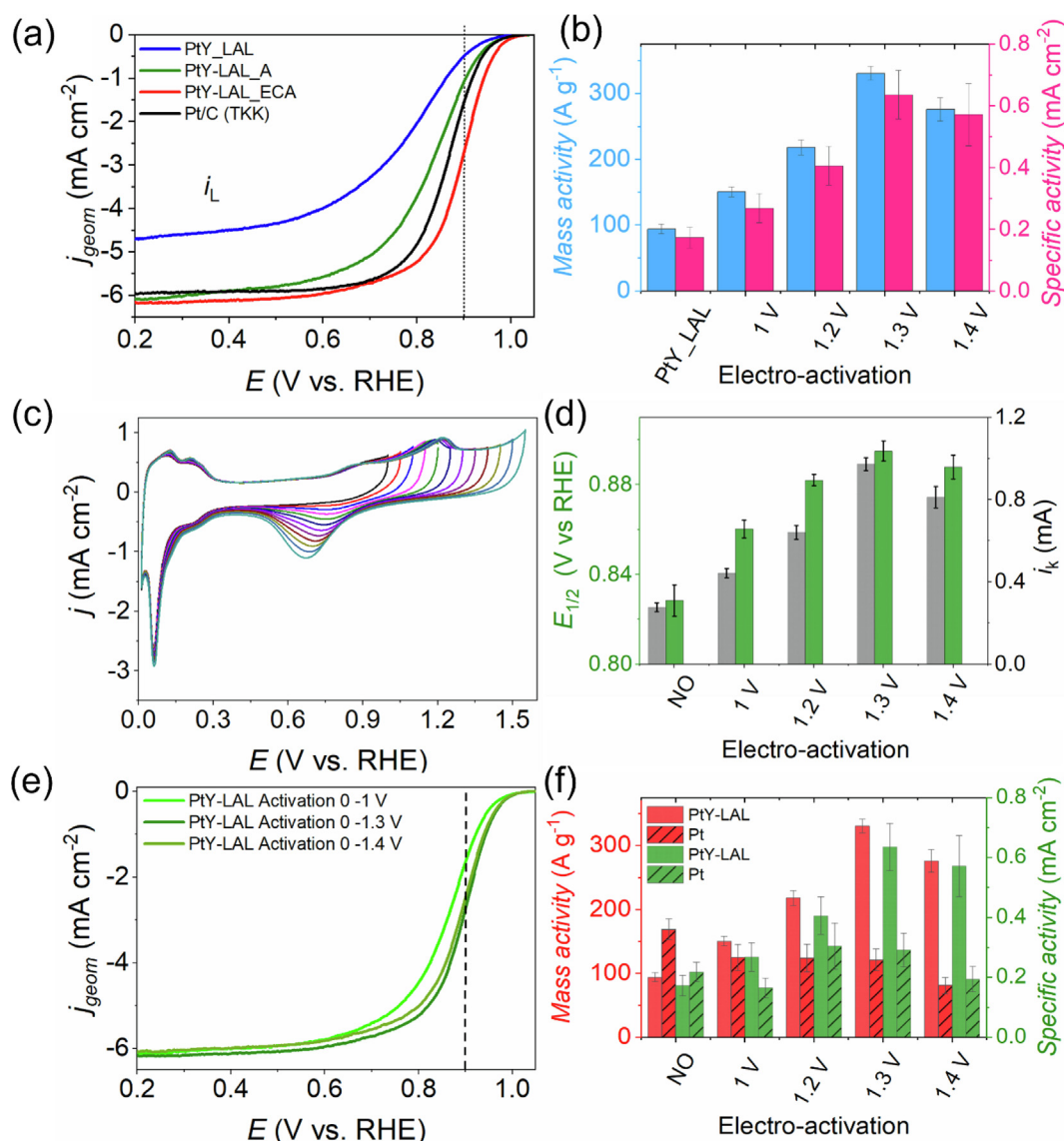

Fig. 4. Chemical and electrochemical activation of PtY-LFL_A electrocatalyst. (a) LSV at RDE recorded at 20 mV s^{-1} and 1600 r min^{-1} in O_2 saturated electrolyte of PtY as prepared, after chemical activation in H_2SO_4 1 M, 10 min 25 °C and after further electrochemical activation in 0.1 M $HClO_4$ for 50 cycles at 200 mV s^{-1} at inversion potential of 1.3 V vs RHE, (b) MA and SA and (d) half wave potential and kinetic current at 0.9 V vs. RHE variation upon electrochemical activation of PtY in 0.1 M $HClO_4$ for 50 cycles at 200 mV s^{-1} at different inversion potentials. (c) Cyclic voltammetry at different inversion potential of PtY-LFL_A catalyst in Ar saturated 0.1 M $HClO_4$ solution recorded at 50 mV s^{-1}, (e) LSV at RDE recorded at 20 mV s^{-1} and 1600 r min^{-1} in O_2 saturated electrolyte of PtY activated by electrochemical cycling at different inversion potential, (f) comparison of MA and SA variation upon electrochemical activation between PtY and Pt.

and the TKK reference. The reason for this bell-shaped trend of activation can be explained by observing the CV response of the catalyst shown in Fig. 4(c). The CV shows the typical Pt electrochemical behavior composed of the hydrogen adsorption/desorption region ($E < 0.3$ V vs. RHE, H_{UPD} region), the capacitive region ($0.3 < E < 0.7$ V vs. RHE) and the reversible PtO adsorption region ($0.7 < E < 1.3$ V vs. RHE, OH_{ads}), where the reversible oxide stripping corresponds to the peak approximately at 0.7 V vs. RHE in the reverse cathodic scan. During the electrochemical activation there is again the capability to dissolve the superficial yttria because of the acid electrolyte, but also other dynamics occurs. In particular the maximum activation is obtained only if the oxygen adsorption region is included in the cycling window range, meaning that PtO layer is formed and destroyed cyclically. This clearly leads to a surface reconstruction and roughening that increases the exposition of active sites and more in general of the surface active area. However, pushing the activation to even higher potentials, such as 1.4 V, leads to a loss of activity because of irreversible phenomena such as ripening and coalescence of Pt NPs as well as leaching of Pt with subsequent redeposition to form larger Pt aggregates. It is important to emphasize that both chemical and electrochemical activation effects are crucial for a marked increase in performance, and this is specific for the PtY alloy. In fact, as can be seen from Fig. 4(f), the increase in activity following electrochemical activation for Pt NPs, obtained under the same laser ablation conditions as PtY_LAL, is little or even negligible. This can be taken as a confirmation that the activation protocol has the function of exposing the Pt_xY metal phase by removing part of the yttria shell.

Having defined an electrochemical activation procedure, this was extended to all catalysts produced by laser ablation and subsequent laser fragmentation in liquid. Fig. 5 shows the electrochemical characterization of the different catalysts and the kinetic analysis for oxygen reduction in 0.1 M $HClO_4$. Fig. 5(a) shows the cyclic voltammetry recorded at 20 mV s^{-1} in argon saturated electrolyte, the H_{upd} region ($E < 0.3$ V vs. RHE) shows well-defined hydrogen adsorption–desorption peaks. The adsorption/desorption features are consistent with the presence of Pt(110) (0.05–0.15 V and 0.23–0.35 V) and Pt(111) sites (0.04–0.35 V) [47]. It is worth stressing that, in ablated samples, the O_{UPD} region is shifted towards more positive potentials. Such an effect can be associated with a less effective adsorption of OH groups on Pt_xY surfaces than on Pt/C, that is the desired effect since O_2 can adsorb at higher potentials with a consequence reduction of the overpotential for O_2 reduction. The positive shift for Pt–OH formation can be due to both strain and ligand effects, which induce the downshifting of the d-band center and in turn affect the adsorption binding energy to adsorb OH [48].

Fig. 5(b) reports the LSV at RDE in O_2 saturated electrolyte while Table 1 resumes the electrochemical data obtained from the kinetic analysis. To extract the ORR activity of the catalysts, the potential was corrected for the ohmic drop (measured via EIS at OCV in O_2-saturated electrolyte). Subsequently, the measured current was extracted at 0.9 V vs. RHE and corrected for the capacitive contribution (determined from a CV in Ar-saturated electrolyte at the same potential). It is evident that all the catalysts are more active than the Pt/C TKK standard but what is interesting is that there is a variation of activity passing from PtY-LFL_A to PtY-LFL_B and PtY-LFL_Bx2, where PtY-LFL_B ($E_{1/2} = 0.943$ V) is the best performing with the most positive $E_{1/2}$. Similarly, the mass transfer kinetic currents determined at 0.9 V vs. RHE attest a superior activity for PtY-LFL_B ($j_k = 15.1$ mA cm^{-2}) followed by PtY_LFL_Bx2, PtY_LFL_A and Pt/C TKK (Table 1).

Tafel analysis of the electrochemical data obtained by LSV was evaluated and is reported in Fig. S5. Typical values of Tafel slope for ORR at polycrystalline Pt electrodes in perchloric acid, range between 60 and 120 mV dec^{-1}, depending on factors such as anion

adsorption, oxide layer formation, uncompensated resistance, and appropriate selection of boundaries for linear fitting. Tafel slopes in the range 60–120 mV dec^{-1} indicates the initial electron transfer to O_2 as rate determining step. The variability of this value over a certain potential range depends in particular on the state of the electrode surface, and especially on the presence or absence of adsorbed oxygen. Pt/C exhibited a Tafel slope of 59 mV dec^{-1}, consistent with literature reports. PtY-LFL_B displayed Tafel slopes of 61 mV dec^{-1}, indicating a low oxygen coverage on the Pt surface and faster kinetics for ORR compared to PtY-LFL_A (69 mV dec^{-1}) and PtY- LFL_Bx2 (68 mV dec^{-1}). Since Tafel slopes of similar magnitude suggest a comparable reaction mechanism and rate-determining steps among different electrocatalysts, it can be asserted that Pt_xY catalysts and the TKK standard share the same mechanism and rate-determining step for ORR.

The electrochemical active area (ECSA) was determined by CO stripping technique (Fig. 5c). Pt/C TKK shows a single well-defined stripping peak, whereas the Pt_xY series displays, at a different extent, multiple CO oxidation peaks, which are mainly attributed to the surface heterogeneity and oxophilicity difference. The first derivative $\partial I/\partial E$, with I being the current and E being the potential, in the Fig. 5(d) provides evidence for the existence of multiple peaks in the case of Pt_xY samples. The wide pre-peak (0.35–0.60 V) is appointed to the desorption of CO from bridge sites at (111) surface [49,50]. Following peak I in the voltammogram there is a further much larger current peak II (Fig. 5c) which is associated with CO adsorbed on terrace of Pt(111) surface [49,50]. The attribution of the additional peak labelled as III is debated in literature reports, where it was attributed to the presence of (100) oriented surface facets, which possess different CO_{ad} oxidation characteristics [50], or to CO oxidation on smaller Pt nanoparticles [51]. However, TEM analysis evidenced smaller nanoparticles in PtY-LFL-B sample, which is the catalyst showing the lowest intensity for the peak III (Fig. 5c, blue curve). Therefore, we hypothesized that peak III is responsible for CO stripping from step sites [52]. The CO stripping measurements point out a similar electrochemical active surface area (ECSA) for the tested electrocatalysts with a slight increase in PtY-LFL_B and PtY-LFL_Bx2 samples with respect to the Pt/C standard (Table 1). ECSA combined with the kinetic current determined at 0.9 V vs. RHE allows to determine the specific activity. This parameter is by far the most indicative of the electrocatalyst performance, as it is based on the effective fraction of Pt that is involved in the catalytic process. Fig. 5(e) reports the specific activity (SA) values for the different catalysts before and after the chemical and electrochemical activation. While the trend remains very similar in both cases, what is evident is the remarkably high SA of the ablated electrocatalysts, surpassing the Pt/C standard by a factor of 3 to almost 5 in the case of PtY-LFL_B. The exceptionally high value of SA for PtY-LFL_B (1.095 mA cm^{-2}), as determined at RDE, attests this electrocatalyst among the most active catalysts as reported in literature such as Pd@PtNi nanowires (SA = 3.18 mA cm^{-2}) [53], PtNi on nitrogen doped carbon (SA = 2.5 mA cm^{-2}) [54]. This SA value has also the same order of magnitude found for Pt_xY NPs synthesized in ultra-high vacuum conditions [5]. In the case of Pt, the mass activity (MA) represents a further important technological parameter, as it allows the catalyst loading of gas diffusion electrode, in PEMFC, to be precisely designed according to expected performance also in relation to cost and availability of critical raw materials such as Pt. Fig. 5(f) reports the MA values for the different catalysts before and after the chemical and electrochemical activation. These values are expressed as the kinetic current at 0.9 V vs. RHE and are normalized by the mass (in mg) of Pt as determined by ICP-MS. The MA value for PtY-LFL_B (1 A mg^{-1}) rises above those of the other tested catalysts, and is comparable with those of the most active model electrocatalysts reported in literature, i.e.
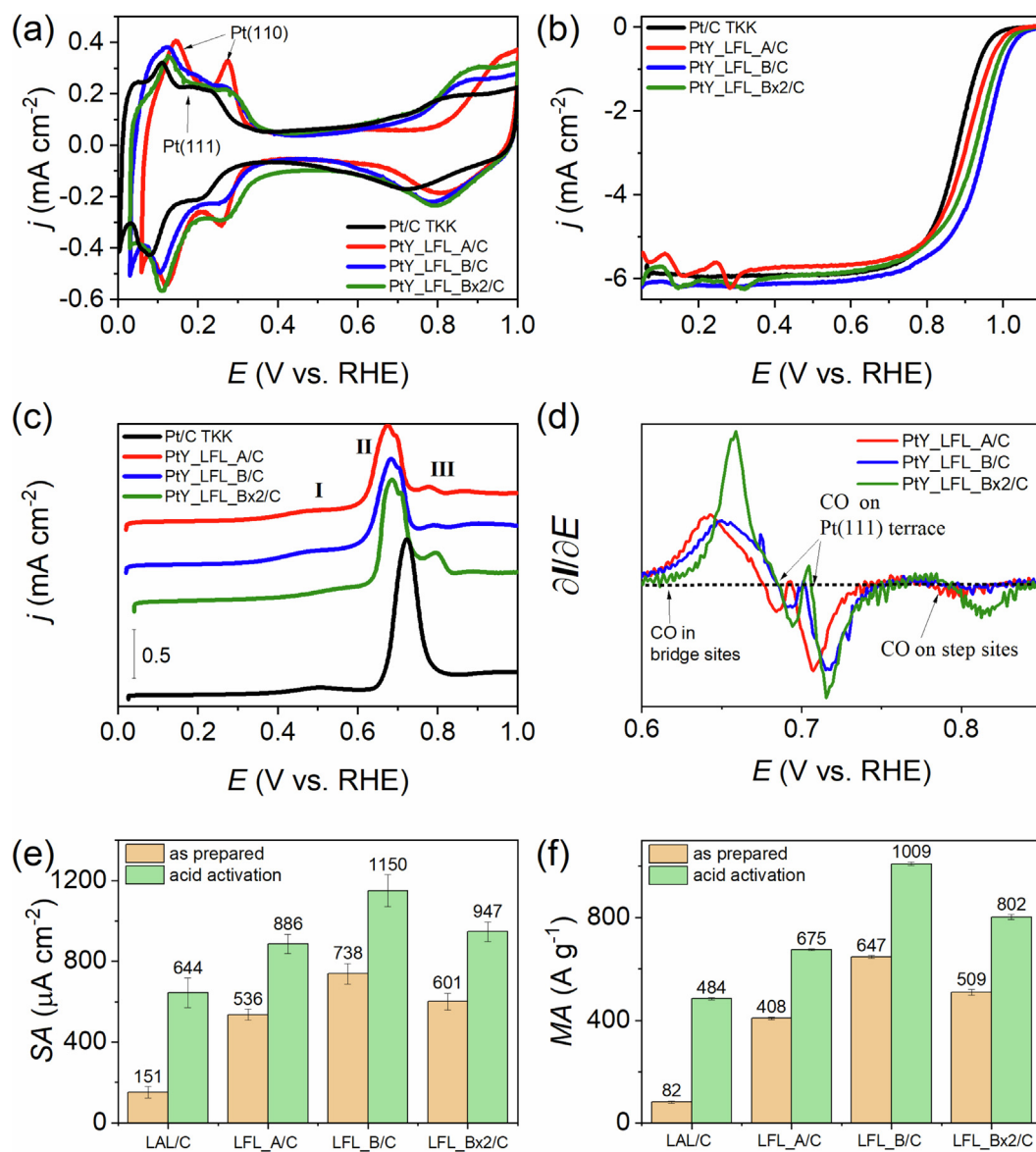
Fig 5. Electrocatalytic performance toward ORR of the evaluated catalysts with the RDE technique. (a) Cyclic voltammetry recorded at 50 mV s^{-1} in Ar saturated 0.1 M HClO$_4$ solution, (b) LSV at RDE recorded at 20 mV s^{-1} and 1600 r min^{-1} in O$_2$ saturated electrolyte, (c) CO stripping performed by CV at 20 mV s^{-1} in Ar saturated 0.1 M HClO$_4$ for, (d) first derivative of CO stripping region of Fig. 4e, (e) Specific activity and (f) mass activity of the as prepared PtY catalysts before and after acid activation,

Table 1
Electrochemical data from kinetic analysis at RDE and GDE electrodes for the investigated electrocatalysts.

	EPSA[a] cm^2	ECSA m^2 g^{-1}	$E_{1/2}$[b] V vs. RHE	j_k[c] mA cm^{-2}	MA[d] A g^{-1}	SA[e] µA cm^{-2}	E_{GDE}[f] V vs. RHE	$j_{k,GDE}$[g] mA cm^{-2}	MA[h] A mg^{-1}
Pt/C TKK	2.36 ± 0.16	80 ± 5	0.867	3.1 ± 0.1	203 ± 5	253 ± 23	0.815	69 ± 5	6900
PtY_LFL_A	2.43 ± 0.28	83 ± 9	0.921	10.1 ± 0.15	675 ± 3	817 ± 98	0.786	98 ± 5	9800
PtY_LFL_B	2.71 ± 0.26	92 ± 9	0.943	15.1 ± 0.1	1009 ± 7	1095 ± 113	0.916	112 ± 5	11,200
PtY_LFL_Bx2	2.7 ± 0.2	91 ± 5	0.928	12.0 ± 0.2	801 ± 10	879 ± 63	0.871	37 ± 5	3700

At least nine independent measurements were made for each catalyst: data are reported as mean values and the uncertainty is reported as the standard deviation.

^a Electrochemical platinum surface area evaluated by CO stripping.
^b Associated error is ± 0.005 V.
^c Kinetic current determined at 0.9 V vs. RHE.
^d Mass activity determined at RDE by considering a Pt loading of 15 µg cm^{-2}.
^e Specific activity determined at RDE by considering a kinetic current at 0.9 V vs. RHE.
^f Onset potential determined at 0.01 A cm^{-2} in A-GDE cell, the associated error is ± 0.005;
^g Kinetic current determined in A-GDE cell at 0.65 V vs. RHE.
^h Mass activity determined at GDE by considering a Pt loading of 10 µg cm^{-2}.
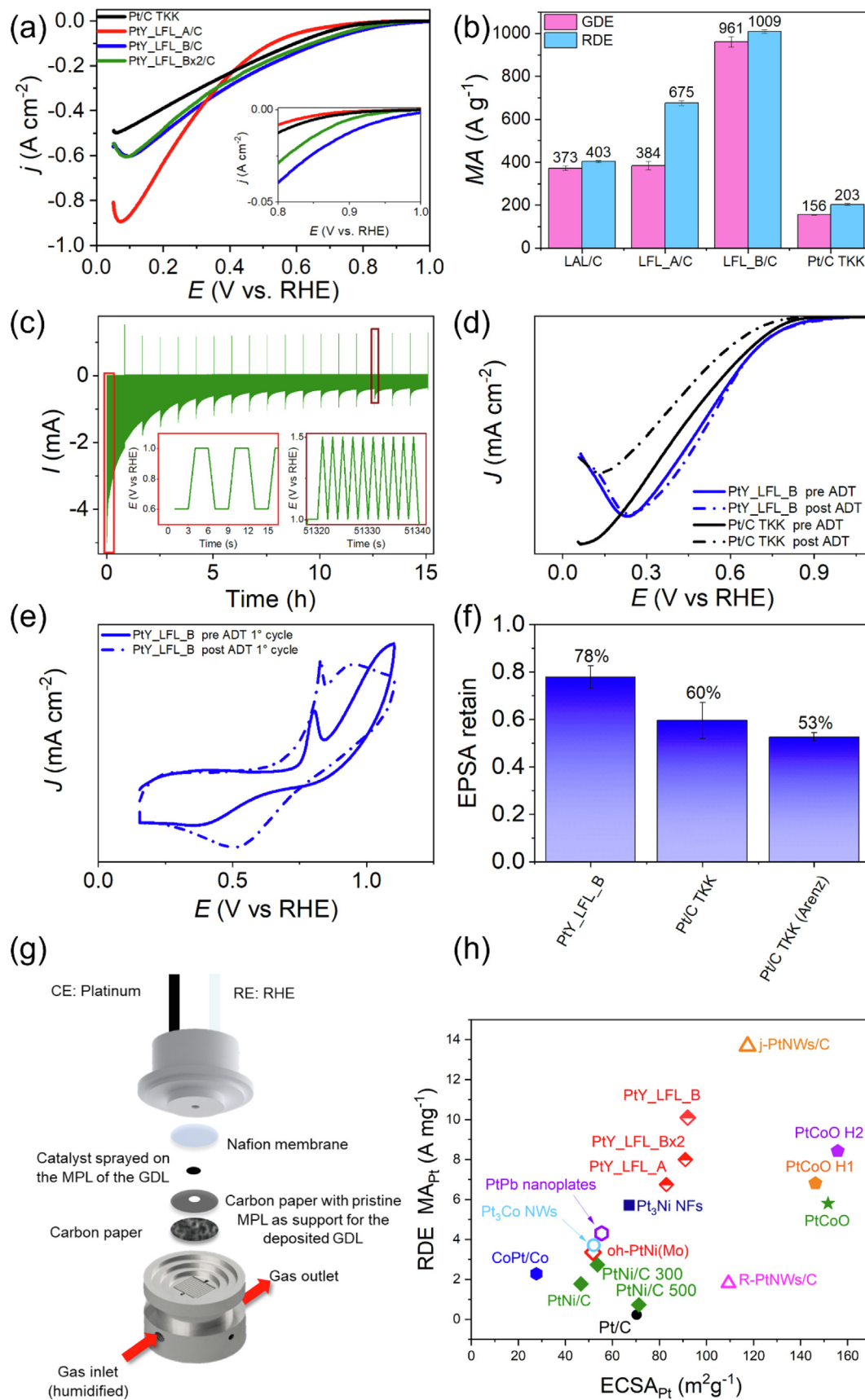
Pd@PtNi nanowires (MA = 1.75 A mg^{-1}) [53], PtNi on nitrogen doped carbon (MA = 2.5 A mg^{-1}) [54], and Pt$_x$Y NPs on glassy carbon (MA = 3.05 A mg^{-1}) [5]. Furthermore, the determined values meet and, in some cases, even exceed current technological Pt ORR mass activity DOE targets (0.44 A mg^{-1}) [55]. However, it is worth to stress that such high mass activities are usually only achieved in the half-cell rotating disc electrode tests, which are affected by mass transport limitation. Clearly, kinetic currents are always corrected by mass-transport (and Ohmic drop) limitations from RDE data, but these corrections become imprecise for potential values below 0.85 V vs. RHE [56].

Although RDE measurements are exceptional for screening electrocatalytic materials and despite tremendous progress in the development procedure for catalyst testing [55,57–61], to date, the performance achieved in the half-cell RDE test are difficult to reproduce in practical PEMFCs; thus, the power density target set by the US DOE for PEFMCs is rarely met or addressed. To surpass this gap without being burdened by complicated experimental conditions and setups as in a PEMFC, a gas diffusion electrode cell (A-GDE), as the one proposed by Arentz & Co, can be adopted [41]. A-GDE cell is used to mimic a proton exchange membrane fuel cell cathode, where the catalysts are loaded on a gas diffusion layer, which is sandwiched between a gas holder and an ion exchange membrane (Fig. 6g). The latter separates the electrolytic solution (4 M HClO$_4$), where the counter and reference electrodes are dipped in Ref. [61]. This setup proved to be useful for the fast screening and testing of low-temperature PEMFC catalysts in experimental condition compatible in term of current density and oxygen concentration as in MEA measurements [62]. Fig. 6 (a) reports the LSV curves of the investigated catalysts at GDE electrode, which confirm the superior activity of PtY-LFL_B in term of onset potential and current in the kinetic potential window (Table 1). For sake of comparison, MA at GDE and RDE determined at 0.9 V vs. RHE are reported in Fig. 6(b), showing a good agreement between the two sets of measurements and specifically for PtY-LFL_B (0.96 A mg^{-1}). Although determining the values at 0.9 V vs. RHE is useful to compare the two experimental approaches (RDE and GDE), as said before, the kinetic current range above 0.85 V vs. RHE is not the region of interest for PEMFC cathodes, and then in this range the current densities are rather smaller if compared to real PEMFC systems. In fact, the kinetic current in GDE set up is typically evaluated at 0.65 V vs. RHE, but beside the absolute values also at this reference potential the activity trend in term mass activity is confirmed (Table 1) [39].

Interestingly, the morphology of the Pt-Y nanoconstruct, i.e., the metal nanoparticles embedded in the Pt-oxide matrix containing also ultrafine Pt, resulted unchanged after the electrocatalysis experiments (Fig. S2) and also after the activation with acid wash (Fig. S3). This finding was confirmed by the XRD of the samples after electrocatalysis experiments (Fig. S4), which is encouraging for addressing the issue of nanocatalysts durability under operating conditions. Hence, the best performing catalyst (PtY-LFL_B) was evaluated through an accelerated degradation test (ADT) based on the one proposed by Arentz & Co (Fig. 6c) [41]. The ADT protocol simulating load cycles consists in a step of 500 potential cycles, where the electrode potential is modulated with a square wave and stepped between 0.6 and 1.0 V vs. RHE with a holding time of 3 s at each voltage (Fig. 6c left insert). The first step is followed by a second one consisting in 10 potential cycles simulating the start-up/shutdown conditions [63], where the electrode potential was cycled with a scan rate of 0.5 V s^{-1} between 1.0 and 1.5 V$_{RHE}$ (Fig. 6c right insert). The two steps are repeated overall 18 times in O$_2$ atmosphere. Fig. 6(d) reports the LSV of PtY-LFL_B electrocatalysts before and after the ADT and it is in plain view that the two electrochemical profiles are almost superimposable, confirming the high stability of the catalyst along with the superior activity with respect to the Pt/C TKK standard previously pointed out. For the purpose of comparison, the LSV profile before and after the ADT test of Pt/C is presented, clearly illustrating the decrease in current (point-dotted line) and consequently, a decline in performance for the Pt/C electrocatalysts following the electrochemical workload. This confirms the hypothesis that the platinum oxide matrix may indeed give the catalyst greater stability, beyond the activity that is attributable to the composition, size and strain of the alloyed nanoparticles. To have a further confirmation about the PtY-LFL_B stability, the EPSA was determined before and after the ADT by conducting CO stripping voltammetry. For the CO stripping measurement, the catalyst was maintained at 0.05 V, and the GDL underwent a 90 s poisoning process with CO followed by a purging of 510 s with Ar. Fig. 6(e) reports the CO stripping CV for PtY-LFL_B (see supporting information for Pt/C). This shows a different response of the catalyst layer before and after the test, such as a higher capacitive current, and an apparent higher peak for formation and stripping of Pt oxide. However, looking at the CO stripping charge and the resulting electrochemically active area obtained before and after the ADT, one can observe that the active surface area loss is only 22% with a surface area retention of 78% as opposed to the 60% observed for Pt/C TKK (53% if we consider the test produced by Arentz & Co. Fig. 6f) [41].

5. Discussion

An integrated laser assisted method was successfully exploited for the optimization of active and stable catalysts for oxygen reduction reaction. These catalysts are based on nanostructured Pt alloys, which are to date the best available systems in terms of activity. The procedure started from a bulk Pt alloy target (Pt$_2$Y 66 wt%, Pt$_3$Y 29 wt%, Pt 5 wt%), providing Pt alloy nanocrystals embedded in a Pt oxide matrix. This special morphology resulted effective in providing the convenient activity and stability performance required towards the implementation in fuel cells. Some of the most relevant electrocatalysts reported in literature for ORR and screened by RDE are reported in Fig. 6(h) and are compared with the PtY electrocatalysts proposed in this paper. It is interesting to observe that PtY-LFL_B stems in term of mass activ-

Fig. 6. Electrocatalytic performance toward ORR of the evaluated catalysts with the GDE technique, (a) LSV at Gas Diffusion Electrode recorded in 4 M HClO$_4$ at 20 mV s^{-1}. (b) Mass activity of PtY catalysts at GDE test cell compared to mass activity as determined by RDE analysis. Accelerated degradation test of PtY_LFL_B/C catalyst with A-GDE electrochemical cell. (c) Current vs. time response of the accelerated stress test. Inserts are the two different potential wave steps applied in the stress protocols. (d) LSV of PtY-LFL_B and Pt/C TKK recorded at A-GDE cell, at 100 mV s^{-1}, before (solid line) and after (dash-spot line) the ADT. (e) CO stripping performed by CV at 50 mV s^{-1} after purging the PtY-LFL_B GDL layer with Ar, before (solid line) and after (dash-spot line) the ADT. (f) EPSA retains for the PtY-LFL_B sample compared with the Pt/C TKK and with the result obtained by Arentz& Co [41]. (g) GDE cell set-up (h) MAs at 0.9 V$_{RHE}$ as a function of ECSAs from RDE measurements of reference materials reported in literature and PtY catalysts reported here. Catalysts include, PtNi nanoframes, Pt$_3$Co nanowires, CoPt/Co, PtPb nanoplates, Pt nanowires (R- PtNWs and J-PtNWs), PtNi/C (and treated 300 and 500 °C), PtCoO, PtCoO H1, PtCoO H2 (PtCoO treated at 573 K for 8 and 16 min, respectively), PtNi(Mo) [64].
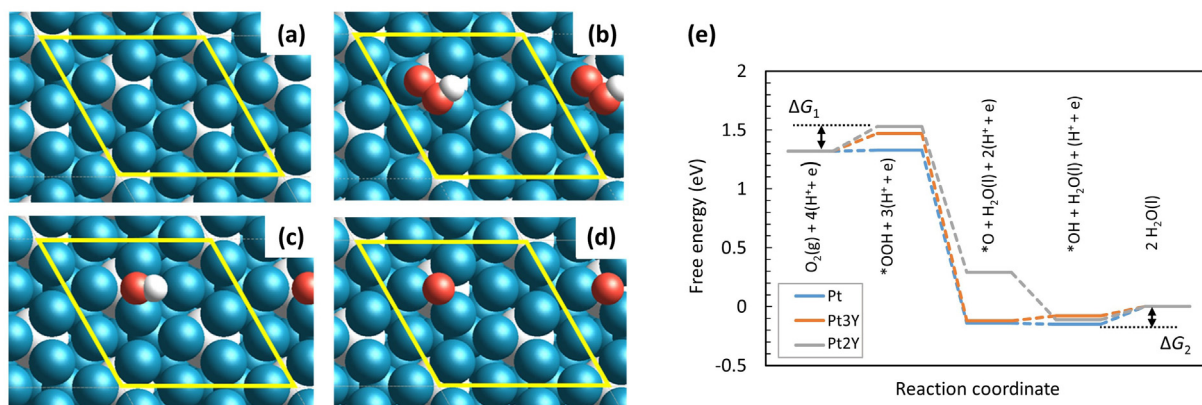
Fig. 7. Top views showing (a) the $\sqrt{3} \times \sqrt{3}R30°$ supercell of the modified $Pt_2Y(111)$ surface and (b) the *OOH, (c) the *O and (d) the *OH intermediates. Blue spheres are Pt atoms, white spheres are Y atoms, red spheres O atoms, small white spheres H atoms. (e) Calculated free energy diagram for the oxygen reduction reaction at 0.9 V (associative path) with respect to the reversible hydrogen electrode under standard conditions for Pt(111) and Pt-covered $Pt_2Y(111)$ and $Pt_3Y(111)$ surfaces.

ity over several Pt alloyed electrocatalysts such as Pt_3Ni nanofoams or Pt_3Co nanowires and approaches values obtained for the Pt nanowires [64]. PtY-LFL_B shows ECSA comparable with Pt_3Ni nanoframes [65] and PtNi/C and not much below self-supported PtCoO [66]. This comparison allows to state that PtY prepared by laser fragmentation in liquid produces electrocatalysts with electrocatalytic properties among the best reported for RDE characterization.

The crystalline component of the best performing sample (PtY-LFL_B) was of 19 wt% of Pt_3Y, 56 wt% of Pt_2Y and 25 wt% of fine Pt, the latter being prevalently at NPs surface according to the XPS analysis. The activity of Pt-Y alloys depends on their stoichiometry but also on the surface composition of the real samples, which in this case is richer in Pt considering the acid wash and the ORR operating conditions. In this regard, DFT-optimized models show that the $Pt_2Y(111)$ and $Pt_3Y(111)$ surfaces are fairly similar, both exposing a Kagome layer of Pt atoms whose holes are filled by Y atoms (see Fig. S9c and d). However, whereas in the case of Pt_3Y, Y atoms are in the same plane of the Pt layer, in Pt_2Y they are located ~1 Å deeper. It is commonly assumed that the surface of actual Pt_xY crystals is depleted of yttrium ("platinum skins") [67]. Hence, we modified the slabs of both systems by replacing the exposed Y atoms by Pt atoms. Interestingly, in the $Pt_2Y(111)$ case these new Pt atoms move outwards, vertically aligning to the other atoms of the Pt skin (see Fig. S9b). Thus, both the Pt_2Y (111) and the $Pt_3Y(111)$ skins have eventually the aspect of a Pt (111) film, but the strain is opposite in the two cases, i.e. compressive (−3%) for the former and expansive (+4%) the latter. As noted by Greeley et al. [67], in the Pt_3Y case the atoms of the Pt skin having only Pt neighbors bind O too strongly. These sites were therefore blocked by O atoms. We computed the free-energy profile of the ORR at T = 298.15 K, p = 1 bar, pH = 1 and E = 0.9 V by shifting the binding energies of the intermediates relative to Pt values computed by Greeley et al. [67].

The ORR associative mechanism proceeds through four steps in which the initially adsorbed $*O_2$ molecule is progressively reduced to *OOH, *OH + $H_2O_{(I)}$, *O + $H_2O_{(I)}$ and finally to 2 $H_2O_{(I)}$. In all the cases, the most stable site corresponds to a Pt atom close to a sub-surface Y atom, see Fig. 7.

It has been pointed out that in this process there are two relevant barriers, i.e., the one relative to the reduction of O_2 to *OOH (ΔG_1) and the one relative to the reduction of *O/*OH to H_2O (ΔG_2) [67]. The free energy diagram obtained for the three surfaces computed for a potential of 0.9 V are reported in Fig. 7(e). The curve of $Pt_3Y(111)$ shows that Pt_3Y has higher ΔG_1 barrier than Pt (0.15 eV vs. 0.01 eV) but lower ΔG_2 barrier (0.12 eV vs.

0.15 eV). The curve related to the reduction process on $Pt_2Y(111)$ shows an even larger value for ΔG_1 (0.21 eV) and a slightly lower value for ΔG_2 (0.11 eV) than Pt. This behavior is coherent with the result that the O adsorption energy (ΔE_O) at the Pt skin of Pt_2Y is 0.6 eV weaker than at the Pt(111) surface, which places Pt_2Y at the far right side of the Volcano plot, as reported by Norskov [67]. This particularly low binding energy of the O species can be in turn traced back to the negative strain of the Pt skin [68]. These results indicate that Pt_3Y and Pt are expected to contribute more than Pt_2Y to the catalytic properties in the ideal conditions of a monolayer thin Pt skin. However, the acid treatment and the ORR operating conditions contribute to the significant impoverishment of Y at the surface of nanocrystals, hence the high activity observed experimentally is in agreement with the DFT predictions for the Pt-rich active surfaces assessed with the XPS analysis.

6. Conclusions

In summary, a synergistic laser ablation and laser fragmentation in liquid approach was used for tuning the size of Pt-Y alloy nanocrystals towards the optimal features of ORR catalysts. The resulting Pt-based nanocrystals were embedded in a Pt oxide matrix which acted efficiently against fine particles coalescence while, at the same time, providing superior robustness compared to standard commercial Pt/TKK. The ORR performance of the laser-optimized Pt-Y nanoalloys resulted in a remarkable activity with $E_{1/2}$ = 0.943 V vs. RHE, a specific activity of 1095 μA cm^{-2} and a mass activity >1000 A g^{-1}, always higher than the commercial Pt TKK catalysts. The accelerated stress tests approaching the operation of real fuel cells evidenced a 18% greater stability than Pt/TKK directly verified on a gas diffusion electrode. This study contributes to the development of feasible and advantageous preparation methods for active yet stable ORR catalysts, which are close to what is required for exploitation in the fuel cells of everyday technology.

Materials availability

All materials generated in this study are available from the lead contact without restriction.

Data and code availability

The datasets generated during this study are available upon specific request to lead contact.

Appendix A. Supplementary data

Supplemental experimental procedures, Figs. S1–S9, Tables S1-S3. Supplemental computational characterization.

Supplementary data to this article can be found online at https://doi.org/10.1016/j.jechem.2023.12.031.

References

[1] B.G. Pollet, S.S. Kocha, I. Staffell, Curr. Opin. Electrochem. 16 (2019) 90–95.
[2] M. Escudero-Escribano, A. Verdaguer-Casadevall, P. Malacrida, U. Grønbjerg, B. P. Knudsen, A.K. Jepsen, J. Rossmeisl, I.E.L. Stephens, I. Chorkendorff, J. Am. Chem. Soc. 134 (2012) 16476–16479.
[3] J. Fichtner, B. Garlyyev, S. Watzele, H.A. El-Sayed, J.N. Schwämmlein, W.J. Li, F. M. Maillard, L. Dubau, J. Michalička, J.M. Macak, A. Holleitner, A.S. Bandarenka, ACS Appl. Mater. Interfaces 11 (2019) 5129–5135.
[4] S.G. Peera, T.G. Lee, A.K. Sahu, Sustain. Energy Fuels 3 (2019) 1866–1891.
[5] P. Hernandez-Fernandez, F. Masini, D.N. McCarthy, C.E. Strebel, D. Friebel, D. Deiana, P. Malacrida, A. Nierhoff, A. Bodin, A.M. Wise, J.H. Nielsen, T.W. Hansen, A. Nilsson, I.E.L. Stephens, I. Chorkendorff, Nat. Chem. 6 (2014) 732–738.
[6] M. Escudero-Escribano, P. Malacrida, M.H. Hansen, U.G. Vej-Hansen, A. Velazquez-Palenzuela, V. Tripkovic, J. Schiotz, J. Rossmeisl, I.E.L. Stephens, I. Chorkendorff, Science 352 (2016) 73–76.
[7] S. Jong Yoo, S.K. Kim, T.Y. Jeon, S. Jun Hwang, J.G. Lee, S.C. Lee, K.S. Lee, Y.H. Cho, Y.E. Sung, T.H. Lim, Chem. Commun. 47 (2011) 11414.
[8] M. Tsuji, K. Uto, T. Nagami, A. Muto, H. Fukushima, J.I. Hayashi, ChemCatChem 9 (2017) 962–970.
[9] Y. Luo, A. Habrioux, L. Calvillo, G. Granozzi, N. Alonso-Vante, Chemphyschem 15 (2014) 2136–2144.
[10] V. Perazzolo, G. Daniel, R. Brandiele, L. Picelli, G.A. Rizzi, A.A. Isse, C. Durante, Chem. – A Eur. J. 27 (2021) 1002–1014.
[11] D. G. Brookins, in: 1st Ed. D. G. Brookins, Eh-pH Diagrams for Geochemistry, Ed. Springer Berlin Heidelberg, Berlin, 1988, Vol. 53.
[12] Y. Hu, J.O. Jensen, L.N. Cleemann, B.A. Brandes, Q. Li, J. Am. Chem. Soc. 142 (2020) 953–961.
[13] R. Brandiele, C. Durante, E. Grądzka, G.A. Rizzi, J. Zheng, D. Badocco, P. Centomo, P. Pastore, G. Granozzi, A. Gennaro, J. Mater. Chem. A 4 (2016) 12232–12240.
[14] R. Cui, L. Mei, G. Han, J. Chen, G. Zhang, Y. Quan, N. Gu, L. Zhang, Y. Fang, B. Qian, X. Jiang, Z. Han, Sci. Rep. 7 (2017) 1–10.
[15] R. Brandiele, A. Guadagnini, L. Girardi, G. Dražić, M.C. Dalconi, G.A. Rizzi, V. Amendola, C. Durante, Catal. Sci. Technol. 10 (2020) 4503–4508.
[16] C.A. Campos-Roldán, A. Parnière, N. Donzel, F. Pailloux, P.Y. Blanchard, D.J. Jones, J. Rozière, S. Cavaliere, ACS Appl. Energy Mater. 5 (2022) 3319–3328.
[17] K. Ehelebe, J. Knöppel, M. Bierling, B. Mayerhöfer, T. Böhm, N. Kulyk, S. Thiele, K.J.J. Mayrhofer, S. Cherevko, Angew. Chemie Int. Ed. 60 (2021) 8882–8888.
[18] J.C. Meier, C. Galeano, I. Katsounaros, J. Witte, H.J. Bongard, A.A. Topalov, C. Baldizzone, S. Mezzavilla, F. Schüth, K.J.J. Mayrhofer, Beilstein J. Nanotechnol. 5 (2014) 44–67.
[19] L. Castanheira, W.O. Silva, F.H.B. Lima, A. Crisci, L. Dubau, F. Maillard, ACS Catal. 5 (2015) 2184–2194.
[20] J.C. Meier, C. Galeano, I. Katsounaros, A.A. Topalov, A. Kostka, F. Schüth, K.J.J. Mayrhofer, ACS Catal. 2 (2012) 832–843.
[21] T. Đukić, L. Pavko, P. Jovanovič, N. Maselj, M. Gatalo, N. Hodnik, Chem. Commun. 58 (2022) 13832–13854.
[22] V.O. Mittal, H.R. Kunz, J.M. Fenton, J. Electrochem. Soc. 154 (2007) B652.
[23] V. Perazzolo, E. Grądzka, C. Durante, R. Pilot, N. Vicentini, G.A. Rizzi, G. Granozzi, A. Gennaro, Electrochim. Acta 197 (2016) 251–262.
[24] S.Y. Huang, P. Ganesan, S. Park, B.N. Popov, J. Am. Chem. Soc. 131 (2009) 13898–13899.
[25] W.J. Lee, S. Bera, H. Woo, H.G. Kim, J.H. Baek, W. Hong, J.Y. Park, S.J. Oh, S.H. Kwon, Chem. Mater. 34 (2022) 5949–5959.
[26] R. Kou, Y. Shao, D. Mei, Z. Nie, D. Wang, C. Wang, V.V. Viswanathan, S. Park, I.A. Aksay, Y. Lin, Y. Wang, J. Liu, J. Am. Chem. Soc. 133 (2011) 2541–2547.
[27] T. Binninger, R. Mohamed, A. Patru, K. Waltar, E. Gericke, X. Tuaev, E. Fabbri, P. Levecque, A. Hoell, T.J. Schmidt, Chem. Mater. 29 (2017) 2831–2843.
[28] F. Ando, T. Gunji, T. Tanabe, I. Fukano, H.D. Abruña, J. Wu, T. Ohsaka, F. Matsumoto, ACS Catal. 11 (2021) 9317–9332.
[29] R.C. Forsythe, C.P. Cox, M.K. Wilsey, A.M. Müller, Chem. Rev. 121 (2021) 7568–7637.
[30] D. Zhang, J. Liu, P. Li, Z. Tian, C. Liang, ChemNanoMat 3 (2017) 512–533.
[31] V. Amendola, D. Amans, Y. Ishikawa, N. Koshizaki, S. Scirè, G. Compagnini, S. Reichenberger, S. Barcikowski, Chem. Eur. J. 26 (2020) 9206–9242.
[32] R. Brandiele, V. Amendola, A. Guadagnini, G.A. Rizzi, D. Badocco, P. Pastore, A.A. Isse, C. Durante, A. Gennaro, Electrochim. Acta 320 (2019) 134563.
[33] S. Reichenberger, G. Marzun, M. Muhler, S. Barcikowski, ChemCatChem 11 (2019) 4489–4518.
[34] S. Hu, G. Goenaga, C. Melton, T.A. Zawodzinski, D. Mukherjee, Appl. Catal. B: Environ. 182 (2016) 286–296.
[35] S. Crivellaro, A. Guadagnini, D.M. Arboleda, D. Schinca, V. Amendola, Rev. Sci. Instrum. 90 (2019) 033902.
[36] K. Rossi, G.G. Asara, F. Baletto, ACS Catal. 10 (2020) 3911–3920.
[37] Z. Ma, Z.P. Cano, A. Yu, Z. Chen, G. Jiang, X. Fu, L. Yang, T. Wu, Z. Bai, J. Lu, Angew. Chemie Int. Ed. 59 (2020) 18334–18348.
[38] A. Facchin, M. Zerbetto, A. Gennaro, A. Vittadini, D. Forrer, C. Durante, ChemElectroChem 8 (2021) 2825–2835.
[39] M. Inaba, A.W. Jensen, G.W. Sievers, M. Escudero-Escribano, A. Zana, M. Arenz, Energy Environ. Sci. 11 (2018) 988–994.
[40] S. Alinejad, M. Inaba, J. Schröder, J. Du, J. Quinson, A. Zana, M. Arenz, J Phys: Energy 2 (2020) 024003.
[41] J. Schröder, V.A. Mints, A. Bornet, E. Berner, M. Fathi Tovini, J. Quinson, G. K. H. Wiberg, F. Bizzotto, H. A. El-Sayed, M. Arenz, JACS Au 1 (2021) 247–251.
[42] J. Du, J. Quinson, A. Zana, M. Arenz, ACS Catal. 11 (2021) 7584–7594.
[43] P. Giannozzi, S. Baroni, N. Bonini, M. Calandra, R. Car, C. Cavazzoni, D. Ceresoli, G.L. Chiarotti, M. Cococcioni, I. Dabo, A. Dal Corso, S. de Gironcoli, S. Fabris, G. Fratesi, R. Gebauer, U. Gerstmann, C. Gougoussis, A. Kokalj, M. Lazzeri, L. Martin-Samos, N. Marzari, F. Mauri, R. Mazzarello, S. Paolini, A. Pasquarello, L. Paulatto, C. Sbraccia, S. Scandolo, G. Sclauzero, A.P. Seitsonen, A. Smogunov, P. Umari, R.M. Wentzcovitch, J. Phys. Condens. Matter 21 (2009) 395502.
[44] D. Vanderbilt, Phys. Rev. B 41 (1990) 7892–7895.
[45] J.P. Perdew, K. Burke, M. Ernzerhof, Phys. Rev. Lett. 77 (1996) 3865–3868.
[46] R. Brandiele, M. Zerbetto, M.C. Dalconi, G.A. Rizzi, A.A. Isse, C. Durante, A. Gennaro, ChemSusChem 12 (2019) 4229–4239.
[47] R. Gómez, J.M. Orts, B. Álvarez-Ruiz, J.M. Feliu, J. Phys. Chem. B 108 (2004) 228–238.
[48] J. Roques, A.B. Anderson, V.S. Murthi, S. Mukerjee, J. Electrochem. Soc. 152 (2005) E193.
[49] G. Samjeské, K. Komatsu, M. Osawa, J. Phys. Chem. C 113 (2009) 10222–10228.
[50] P. Urchaga, S. Baranton, C. Coutanceau, G. Jerkiewicz, Langmuir 28 (2012) 3658–3663.
[51] Y.E. Seidel, M. Müller, Z. Jusys, B. Wickman, P. Hanarp, B. Kasemo, U. Hörmann, U. Kaiser, R.J. Behm, J. Electrochem. Soc. 155 (2008) K171.
[52] I.J. McPherson, P.A. Ash, L. Jones, A. Varambhia, R.M.J. Jacobs, K.A. Vincent, J. Phys. Chem. C 121 (2017) 17176–17187.
[53] Y. Zhao, L. Tao, W. Dang, L. Wang, M. Xia, B. Wang, M. Liu, F. Gao, J. Zhang, Y. Zhao, Small 15 (2019) 1900288.
[54] Q. Feng, X. Wang, M. Klingenhof, M. Heggen, P. Strasser, Angew. Chemie Int. Ed. 61 (2022) e202203728.
[55] Z. Zhao, M.D. Hossain, C. Xu, Z. Lu, Y.S. Liu, S.H. Hsieh, I. Lee, W. Gao, J. Yang, B. V. Merinov, W. Xue, Z. Liu, J. Zhou, Z. Luo, X. Pan, F. Zaera, J. Guo, X. Duan, W.A. Goddard, Y. Huang, Matter 3 (2020) 1774–1790.
[56] R. Riasse, C. Lafforgue, F. Vandenberghe, F. Micoud, A. Morin, M. Arenz, J. Durst, M. Chatenet, J. Power Sources 556 (2023) 232491.
[57] K. Shinozaki, J.W. Zack, S. Pylypenko, B.S. Pivovar, S.S. Kocha, J. Electrochem. Soc. 162 (2015) F1384–F1396.
[58] S.S. Kocha, K. Shinozaki, J.W. Zack, D.J. Myers, N.N. Kariuki, T. Nowicki, V. Stamenkovic, Y. Kang, D. Li, D. Papageorgopoulos, Electrocatalysis 8 (2017) 366–374.
[59] H.A. Gasteiger, S.S. Kocha, B. Sompalli, F.T. Wagner, Appl. Catal. B Environ. 56 (2005) 9–35.
[60] Y. Garsany, O. Baturina, K.E. a Swider-Lyons, S.S. Kocha, Anal. Chem. 82 (2010) 6321–6328.
[61] M. Mazzucato, C. Durante, Electrochim. Acta 463 (2023) 142801.
[62] K. Ehelebe, N. Schmitt, G. Sievers, A. W. Jensen, A. Hrnjić, P. Collantes Jiménez, P. Kaiser, M. Geuß, Y.P. Ku, P. Jovanovič, K. J. J. Mayrhofer, B. Etzold, N. Hodnik, M. Escudero-Escribano, M. Arenz, S. Cherevko, ACS Energy Lett. 7 (2022) 816–826.
[63] C.A. Reiser, L. Bregoli, T.W. Patterson, J.S. Yi, J.D. Yang, M.L. Perry, T.D. Jarvi, Electrochem. Solid-State Lett. 8 (2005) A273.
[64] Y. Sun, S. Polani, F. Luo, S. Ott, P. Strasser, F. Dionigi, Nat. Commun. 12 (2021) 5984.
[65] V. Beermann, M. Gocyla, S. Kühl, E. Padgett, H. Schmies, M. Goerlin, N. Erini, M. Shviro, M. Heggen, R.E. Dunin-Borkowski, D.A. Muller, P. Strasser, J. Am. Chem. Soc. 139 (2017) 16536–16547.
[66] G.W. Sievers, A.W. Jensen, J. Quinson, A. Zana, F. Bizzotto, M. Oezaslan, A. Dworzak, J.J.K. Kirkensgaard, T.E.L. Smitshuysen, S. Kadkhodazadeh, M. Juelsholt, K.M.Ø. Jensen, K. Anklam, H. Wan, J. Schäfer, K. Čépe, M. Escudero-Escribano, J. Rossmeisl, A. Quade, V. Brüser, M. Arenz, Nat. Mater. 20 (2021) 208–213.
[67] J. Greeley, I.E.L. Stephens, A.S. Bondarenko, T.P. Johansson, H.A. Hansen, T.F. Jaramillo, J. Rossmeisl, I. Chorkendorff, J.K. Nørskov, Nat. Chem. 1 (2009) 552–556.
[68] L. Grabow, Y. Xu, M. Mavrikakis, Phys. Chem. Chem. Phys. 8 (2006) 3369–3374.